Structural behaviour of OP-ROY at extreme conditions

Nicholas P. Funnell, Craig L. Bull, Christopher J. Ridley and Silvia Capelli

Published version information

Citation: NP Funnell et al. "Structural behaviour of OP-ROY at extreme conditions." CrystEngComm, vol. 21, no. 30 (2019): 4473-4483.

DOI: 10.1039/C8CE01946K

Journal Name

ARTICLE TYPE

Cite this: DOI: 10.1039/xxxxxxxxxx

Structural behaviour of OP–ROY at extreme conditions†

Nicholas P. Funnell,* Craig L. Bull, Christopher J. Ridley, and Silvia Capelli

Received Date
Accepted Date

DOI: 10.1039/xxxxxxxxxx

www.rsc.org/journalname

The effects of high pressure and low temperature have been explored on the 'orange-plate' (OP) form of the highly-polymorphic 5-methyl-2-[(2-nitrophenyl)amino]-3-thiophenecarbonitrile molecular crystal structures. Neutron powder and single-crystal diffraction measured up to 9.3 GPa and 40 K, respectively, show that the crystal structure is robust, retaining $P2_1/n$ symmetry over the pressure and temperature range studied, even though it is revealed to be quite soft, having a bulk modulus of 4.3(3) GPa. Intermolecular and lattice energies become progressively less favourable with pressure, relative to the thermodynamically-stable 'yellow' (Y, $P2_1/n$) form, showing that the kinetic barriers to transformation, stabilising the material, persist from ambient to extreme conditions.

1 Introduction

Polymorphism in crystalline materials can present considerable challenges to controlling crystal structure, especially in cases where kinetics dominate over thermodynamics. These difficulties are well-documented, particularly for computational structure prediction where likely candidates are often proposed on the basis of relative thermodynamic stabilities, and also in selective polymorph growth, where subtleties in crystallisation conditions can promote formation of kinetically stable forms instead.[1,2] 5-methyl-2-[(2-nitrophenyl)amino]-3-thiophenecarbonitrile (molecular structure shown in Figure 1) ranks among the most polymorphic organic substances known, where kinetics play a major stabilising role, and is consequently one of the more well-studied molecules in the chemical crystallographic literature.[3–9] It is thought to exhibit at least ten solid forms under ambient conditions, the majority of which exhibit significant metastability which has enabled their full structural characterisation; only two of these now remain undetermined following recent publication of the eighth structure ('R05'-form), solved from powder diffraction data.[10,11] None of the forms have clearly-related crystal structures and are all visually distinct macroscopically, exhibiting different morphologies and colours. The strong variation in colour (red, orange, and yellow), has led to the colloquial 'ROY' name being used to refer to the material in general, where the individual polymorphs are currently named according to their physical characteristics (and sometimes year of discovery), for example 'ORP' refers to the 'orange-red plate' form. Additional complicating factors in the phase behaviour of ROY are its ability to cross-nucleate and that all known phases have been observed to crystallise concomitantly from the melt and solution.[12]

The rich phase behaviour of ROY, coupled with the propensity for multi-gigapascal pressures to drive crystalline transitions, motivated an earlier study by one of us to explore whether pressure could be used to influence the free energy of the 'Y'-form (yellow, $P2_1/n$) crystal structure,[13] potentially overcoming any kinetic metastability that otherwise allows so many of the ROY polymorphs to coexist. Intriguingly, we found that although the material progressively changed colour with increasing pressure, from yellow to red, the crystal packing remained unchanged. This piezochromic behaviour can be ascribed to flexibility inherent to the packing motif, and intramolecular geometry, namely the SCNC torsion angle (hereinafter referred to as 'τ_{SCNC}', and illustrated in Figure 1) which varies by as much as 91° between the most extreme conformations within the ROY family, adopted by the 'YT04' and 'R'-forms.

Although we previously found no crystallographic change in the Y-form under pressure, or temperature (on cooling to 30 K), it is thought to be the most thermodynamically stable of the ROY polymorphs. It is in this context that we turn to another of the ROY phases—the 'OP' (orange-plate, $P2_1/n$) form which is less energetically favoured under ambient temperature and pressure conditions. The Y-form accommodated pressure-induced volume reduction, in part, via significant intramolecular flattening of the molecule whereas in the OP-form, the nitrophenyl and thiophene

ISIS Neutron and Muon Facility, Rutherford Appleton Laboratory, Chilton, U. K.; Tel: +44(0)1235 445385; E-mail: nick.funnell@stfc.ac.uk

† Electronic Supplementary Information (ESI) available: CIFs for all refined structures, Rietveld fits for all pressures, refinement details for all structures, CASTEP-calculated torsion angles and corresponding fits, thermodynamic energy calculations, low-temperature structures showing disordered methyl group orientations, and void-space diagrams. See DOI: 10.1039/b000000x/. CCDC 1878576–1878594.

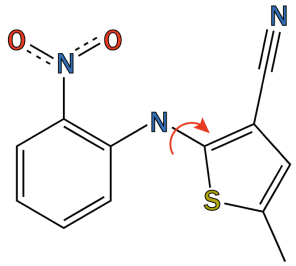

Fig. 1 The molecular structure of 5-methyl-2-[(2-nitrophenyl)amino]-3-thiophenecarbonitrile. The molecule exhibits considerable flexibility about the SCNC dihedral angle τ_{SCNC}, shown with the red arrow. Hydrogen atoms are omitted for clarity.

groups are already closer to co-planarity under ambient conditions, reducing the extent to which the molecule can be deformed, thus forcing the effects of pressure to be taken up elsewhere in the crystal structure. We report the outcome of neutron powder and single-crystal experiments to 9.3 GPa and 40 K, respectively, that aim to probe the stability of the OP phase and contrast its behaviour against that seen in the relatively-stable Y-form.

2 Experimental

2.1 High-pressure neutron powder diffraction

High-pressure neutron powder diffraction data were collected on the PEARL diffractometer at the ISIS neutron and muon facility—details on the PEARL instrument and the associated experimental and data-correction procedures, described in this section, are given in ref. 14. Three separate experiments were peformed; in all cases, a hydrogenous, phase-pure sample of OP ROY (used as supplied by TCI Chemicals) was loaded into a null-scattering, encapsulated, titanium–zirconium gasket[15] with a lead pellet to act as a pressure marker. Hydrostatic compression conditions were achieved by using a perdeuterated methanol–ethanol mixture, in a 4:1 volume ratio. The gasket was loaded in a V3 Paris–Edinburgh (PE) press, equipped with zirconia-toughened alumina (ZTA) anvils for the first two experiments and single-toroidal sintered diamond anvils for the third.[16] Time-of-flight (ToF) diffraction data were collected across the *d*-spacing ranges 0.5–4.1 and 4.2–8.0 Å, the latter achieved by taking advantage of the pulse structure at ISIS and counting the fourth pulse for twice as long as the first three. In the first experiment, data were collected at the following applied loads: 5, 20, 30, 35, 40, 50, and 57.5 tonnes, the second experiment covered the range 5.5–11.5 tonnes in 1 tonne increments, and the third collection was carried out at 95 tonnes. Beam attenuation by the anvils was accounted for using an in-house procedure. Data were normalised against vanadium and absorption-corrected using Mantid.[17]

2.2 Low-temperature neutron single-crystal diffraction

A suitable single crystal of hydrogenated OP ROY for neutron diffraction, measuring approximately $4 \times 3 \times 2$ mm, was grown via slow evaporation of acetone from a saturated solution. Neutron diffraction data were collected on the SXD instrument at the ISIS neutron and muon facility, using the ToF Laue diffraction method.[18] The crystal was attached to the tip of an aluminium pin and mounted in a cryo-cooled refrigerating (CCR) device. Data were collected at 293, 150, 100, 60, and 40 K, measuring each crystal orientation for *ca.* 4, 3, 2.5, 2, and 2 hours, respectively, over a total of five orientations at each temperature. The diffraction peaks were initially indexed with unit cells available from our own unpublished X-ray measurements at the corresponding temperatures. Bragg intensities were extracted using the 3D-profile fitting method implemented in the SXD2001 software[19,20] and corrected for the Lorentz effect.

2.3 Density functional theory calculations

Geometry optimisations were performed using CASTEP 7.0.3 where starting coordinates were taken from preliminary refinements against the powder diffraction data.[21] The unit cell parameters were held fixed to experimentally-determined values and the coordinates were allowed to optimise with $P2_1/n$ symmetry. The PBE exchange-correlation functional was used with the Grimme dispersion correction scheme, along with ultra-soft pseudopotentials.[22–24] Convergence testing of plane-wave cutoff energies and the *k*-point grid size determined optimal values for these of 1200 eV and $3 \times 2 \times 2$ Å^{-1} (OP–ROY) or $3 \times 2 \times 3$ Å^{-1} (Y–ROY), respectively. Relatively stringent convergence criteria were set as follows: total energy per atom, 5×10^{-6} eV Å^{-3}; maximum force, 0.01 eV Å^{-3}; maximum displacement, 5×10^{-4} Å; and maximum stress of 0.02 GPa.

2.4 Intermolecular interaction calculations

Electron densities for ROY molecules at each pressure/temperature were calculated using Gaussian09 at the MP2 level, using a 6-31G(d,p) basis set.[25] Density grid sizes were identified by the pixmt2 module in the PIXEL suite of programs.[26,27] The resulting density files were used with the PIXELC module to calculate intermolecular energies greater than 3 kJmol^{-1}; calculation parameters were all set to default values. Interactions were visualised using the processPIXEL software.[28]

2.5 Normal coordinate analysis

The temperature dependence of the anisotropic displacement parameters (ADPs) from multi-temperature single crystal neutron diffraction was analysed using the Bürgi-Capelli method, as implemented in the program NKA.[29,30] A unique set of normal modes was used to describe the ADPs at all temperatures and the model of motion was defined within an orthogonal coordinate system where the x-axis was aligned with the C7 and C1 atoms (bonded either side of the secondary amine); the y-axis aligned with the amine N-H bond; and the z-axis placed to complete a right-handed Cartesian system.

2.6 Refinement strategies

High-pressure powder data were refined using TOPAS 5.0.[31] Following determination of the unit cell parameters using the Pawley method, preliminary Rietveld refinements were carried out where the molecules were described using a Z-matrix. Single

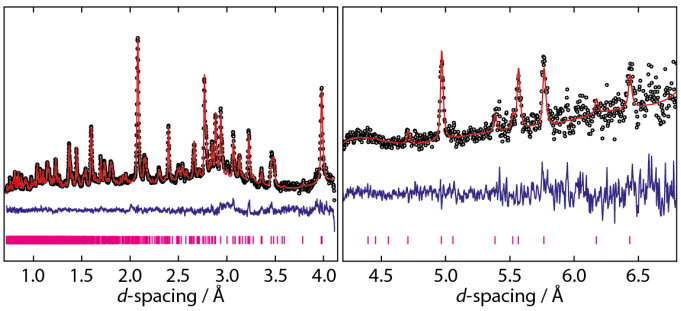

Fig. 2 Rietveld refinement of ROY OP at 5.8 GPa, R_{Bragg}=0.01105; complete fitting statistics are given in Table 1 and in the ESI†. The *d*-spacing ranges over which the data were usable are shown: 0.7–4.1 Å and 4.2–6.8 Å on the left and right, respectively. The full patterns are shown in the ESI†. Data points are shown in black, the fit with a red line and the residual with a blue line. Pink tickmarks indicate reflections from the ROY sample only—indicators for the Pb and ZTA contaminants are omitted for clarity, although these still contribute to the fitted profile. Note that a factor of four in counting statistics and a decrease in neutron flux as a function of increasing wavelength is responsible for the markedly different signal-to-noise between the two fitted regions.

parameters were used for aromatic C–C bonds and angles, N–O bonds,C–H/N–H bonds and C=C/C=S double bonds in the thiophene group. The methyl group was constrained to have C_{3v} point symmetry but allowed to rotate freely. The nitro group was constrained to have C_{2v} symmetry about the C–N axis. Torsion angles that were not constrained to be 0 or 180° according to aromaticity rules were permitted to refine freely. A common isotropic displacement parameter was refined for all non-hydrogen atoms and displacement parameters for hydrogen atoms were set to 1.2× this value. Starting values for all Z-matrix parameters were taken from the previously reported values for OP ROY in the Cambridge Structural Database (CSD refcode: QAXMEH03).[32] Data quality did not permit stable Rietveld refinement at the highest-pressure of 9.3 GPa; only Pawley refinement was possible.

Each dataset was then re-refined, this time using the CASTEP-optimised results to inform restraints on torsional geometry, owing to some insensitivity to these features in the initial refinement—this procedure is discussed in more detail later. Refinement statistics for select pressures are available in Table 1; all datasets can be found in the ESI†. A representative Rietveld fit is shown in Figure 2, for data at 5.8 GPa.

Final cell parameters for the single-crystal data, at each temperature, were refined against the fitted positions of the Bragg reflections after 3D profile integration. The starting models for structural refinement were based on the atomic coordinates of the non-hydrogen atoms from the X-ray structure at room temperature, while all hydrogen atoms were located from neutron Fourier difference maps. At all temperatures except 40 K large negative residual peaks in the difference maps reveled the presence of additional methyl hydrogen atoms, indicating rotational disorder of the group. The disorder was modelled with three possible orientations at 293, 150 and 100 K and two orientations at 60 K, using restraints on the C–H and H···H distances and group isotropic displacement parameters for the hydrogen atoms. Only a single methyl orientation was identified for the 40 K dataset and anisotropic displacement parameters for the hydrogen atoms were used; the resulting ellipsoids were elongated perpendicular to the C–H bond attesting that a non-negligible level of vibration was still present. All structures were refined by full matrix least squares against F^2 using SHELXL.[33] A summary of refinement details and agreement factors is given in Table 1.

2.7 Neutron scattering from hydrogenated materials

Deuterated materials give a superior neutron scattering signal compared to their hydrogenated counterparts, however, in some cases deuteration is not possible, and occasionally undesirable. Substituting hydrogen for deuterium is well-known to modify phase boundary locations, but infrequently it has also been observed to induce isotopic polymorphism,[35–37] and, rarely, a combination of these phenomena.[38] Furthermore, perdeuterated materials may simply be prohibitively difficult to synthesise, as is the case for ROY, having hydrogen atoms in several different chemical environments and a wide variety of functional groups on the molecule. Only the amine hydrogen atom can be exchanged readily using deuterated solvents, and this leads to an increased preference for the Y form.[39] Although neutrons are still sensitive to the hydrogen atom nucleus, this is often obscured by its large incoherent scattering cross-section, resulting in elevated background levels. However, theory suggests that the issues arising from the incoherent contribution can be reduced by using a small sample volume (although this has not clearly been observed experimentally),[40] as is necessarily the case for high-pressure experiments where a typical sample volume for the PE press is *ca.* 66 mm^3 or less. While data quality would certainly be improved if deuteration were possible, successful neutron-powder refinements have been reported for hydrogenous materials.[41,42] The effects of hydrogenation are less severe for single-crystal experiments; the incoherent scattering contributes to the overall background, so integration of a few discrete regions of the diffraction pattern (i.e. the Bragg peaks) only includes a small proportion of the incoherent scatter.

3 Results

3.1 Compression

Up to the maximum pressure measured here, the OP crystal structure remained in the same $P2_1/n$ phase as the ambient form. The unit cell dimensions, reformulated as a set of orthogonal directions $\mathbf{X}_1 \approx \mathbf{a} - 0.1\mathbf{c}$; $\mathbf{X}_2 \approx -0.5\mathbf{a} - 0.9\mathbf{c}$; $\mathbf{X}_3 = \mathbf{b}$, show that the compressibility order is $\mathbf{X}_1 >> \mathbf{X}_2 > \mathbf{X}_3$, decreasing by 19.93, 5.97 and 4.49%, respectively. This led to an overall reduction in cell volume of 28.0%, decreasing from 1199.9(4) Å^3 (ambient pressure dimensions obtained from the CSD—QAXMEH03) to 863.7(7) Å^3. A third-order Birch–Murnaghan equation of state,[43] fitted to the unit cell volume data using PASCal,[44] found the bulk modulus B_0 to be 4.3(3) GPa with $B' = 15.3(9)$ and a refined V_0 of 1214(4) Å^3, indicating a highly-compressible structure. Figure 3 shows plots of the axis compressibility curves and the Birch–Murnaghan fit to the cell volume data. As pressure increases, the molecule flattens relative to its ambient form—a side-by-side

Table 1 Refinement details for select high-pressure and low-temperature data collections. Only Pawley refinement could be performed against the data measured at 9.3 GPa. $R1$ figures of merit are given for single crystal data, R_{Bragg} for Rietveld-refined structures (this has been shown to be more reliable than R_{wp} for neutron powder diffraction on H-containing materials)[34] and R_{wp} for the Pawley refinement at 9.3 GPa, as structural parameters are not available. The use of the Pawley method means reflection intensities can be refined directly, hence the large number of parameters for the data at 9.3 GPa. The differing number of parameters between the remaining data can be ascribed to the need to refine a ZrO_2 impurity phase in some data.

Presssure/temperature	0.109(5) GPa	0.975(5) GPa	2.628(6) GPa	5.842(8) GPa	9.27(16) GPa	150(2) K	40(2) K
Chemical formula	$C_{12}H_9N_3O_2S$	$C_{12}H_9N_3O_2S$	$C_{12}H_9N_3O_2S$	$C_{12}H_9N_3O_2S$	$C_{12}H_9N_3O_2S$	$C_{12}H_9N_3O_2S$	$C_{12}H_9N_3O_2S$
Formula weight / g mol^{-1}	259.29	259.29	259.29	259.29	259.29	259.29	259.29
Crystal system	Monoclinic	Monoclinic	Monoclinic	Monoclinic	Monoclinic	Monoclinic	Monoclinic
a-axis / Å	7.9313(8)	7.4126(4)	6.9954(5)	6.6153(5)	6.3915(13)	7.765(3)	7.651(2)
b-axis / Å	13.313(2)	13.2122(15)	13.0631(18)	12.8681(15)	12.721(7)	13.283(3)	13.243(3)
c-axis / Å	11.6544(17)	11.4253(11)	11.2417(13)	11.0475(12)	10.910(6)	11.615(4)	11.624(4)
β / °	104.509(12)	103.122(7)	102.703(9)	102.894(8)	103.17(3)	104.140(19)	104.118(19)
Volume / Å^3	1191.3(3)	1089.73(17)	1002.1(2)	916.72(17)	863.7(7)	1161.7(6)	1142.2(6)
Density / gcm^{-3}	1.446	1.580	1.719	1.879	1.994	1.482	1.508
τ_{SCNC} / °	41.1(8)	35.3(5)	32.3(6)	28.2(6)	–	44.1(3)	43.2(2)
Measured d-spacing / Å	0.5–4.1, 4.2–8.0	0.5–4.1, 4.2–8.0	0.5–4.1, 4.2–8.0	0.5–4.1, 4.2–8.0	0.5–4.1, 4.2–8.0	0.35–6.5	0.35–6.5
Parameters	57	49	56	57	412	255	249
Unique reflections/data points	3707	3707	3707	3707	2341	7180	9984
$R1/R_{\mathrm{Bragg}}/R_{\mathrm{wp}}$	0.01854	0.01250	0.01558	0.01105	0.01674	0.0673	0.0690
Goodness of fit	0.861	0.777	1.063	1.002	0.683	1.498	1.448
$\Delta\rho_{\mathrm{max}}$, $\Delta\rho_{\mathrm{min}}$ / e Å^{-3}	–	–	–	–	–	1.24, −1.27	2.23, −2.08
Extinction coefficient	–	–	–	–	–	0.0060(3)	0.0080(3)

comparison of the structures at ambient pressure and at 5.8 GPa (the highest pressure for which atomic coordinates could be refined) is shown in Figure 4—where the overall change in torsion angle is 17.9°, decreasing from 46.1° to 28.2°.

3.2 Thermal response

The OP crystal structure remained unchanged down to the lowest measured temperature of 40 K, where the volume decreased by 6.1% from 1216.8(6) Å^3 at 293 K to 1142.2(6) Å^3. Similar to the effect of pressure, reducing temperature led to a small degree of flattening in the molecule via τ_{SCNC}, decreasing from 46.2° to 43.2°. The methyl group was found to exhibit a number of stable conformations being occupationally disordered, where three distinct orientations were identified at 293, 150 and 100 K, two orientations at 60 K and only a single set of atomic positions at 40 K (see ESI† for diagrams). The equidistant spacing between methyl orientations at room temperature implies that this group is freely rotating, which may not have been detected by previous X-ray characterisation, and that thermally-induced contraction of the unit cell reduces the free volume around the methyl group, forcing the H atoms to sit in a unique position on average. The restraints on the high-pressure powder refinements makes it difficult to test for additional methyl hydrogen sites, although the cell volume at 40 K is comparable to that at 0.4 GPa—1146.3(2) Å^3—the methyl group may already have become ordered. However, reorientation of the methyl hydrogen atoms is observed with pressure, where the group rotates by approximately 25° up to 5.8 GPa, likely as a result of avoiding short intermolecular, steric contacts.

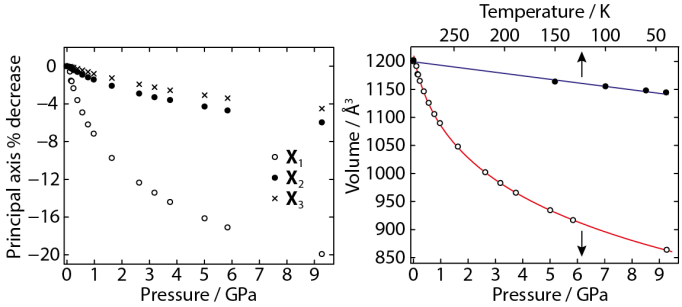

Fig. 3 Left: compressibility of orthogonal directions up to 9.3 GPa. Right: Cell volume as a function of pressure (open circles, lower x-axis) and temperature (filled circles, upper x-axis); the arrows provide a further indication of the relevant graph axis. A third-order Birch–Murnaghan fit to the pressure-dependent unit cell volume data is shown with a red line. The temperature data trend can be approximated with a linear fit, shown in blue (gradient: 0.232(14), intercept: 1130(2), R^2: 0.99). Standard uncertainties on the volume data are within the size of the data points.

4 Discussion

4.1 Restrained Rietveld refinement

While generally successful, some instabilities in the preliminary high-pressure refinements led to our decision to explore DFT as

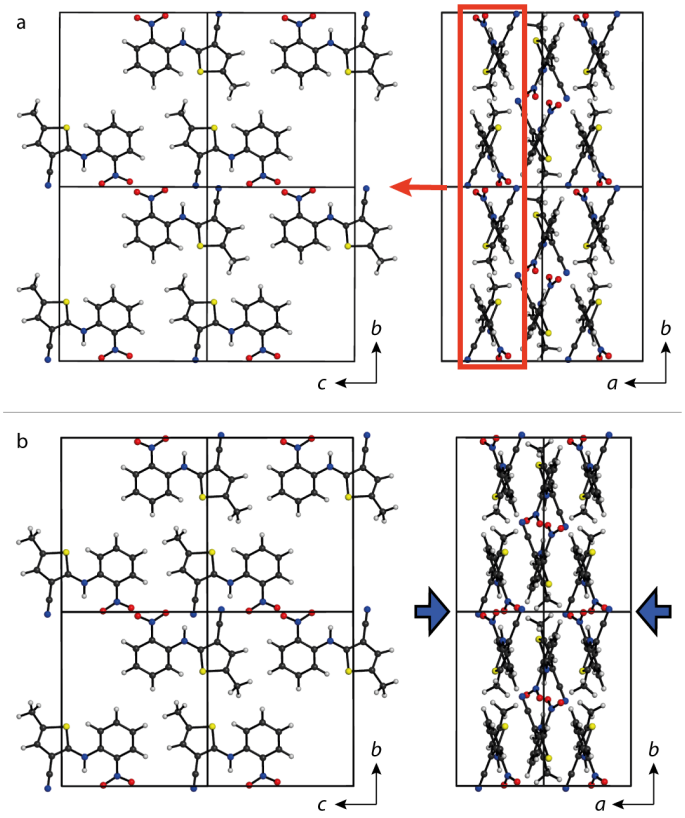

Fig. 4 Refined crystal structures at a) ambient pressure and b) 5.8 GPa. Left and right columns show projections along the *a*- and *c*-axes, respectively. For clarity, only one layer of molecules is shown for the left hand images; the red box in the upper-right graphic highlights these molecules. The blue arrows in the lower right panel emphasise the most pronounced direction of compression on the lattice.

a source of geometric restraints; the usefulness of DFT-informed powder refinements has been demonstrated previously.[45,46] Initial Rietveld refinements showed that a narrow range of values could be adopted by τ_{SCNC} while producing near-equivalent fits to data—although an overall flattening of the molecule was still evident across the pressure series. These refinements were used as the starting point for the optimisations in CASTEP, which also showed a degree of insensitivity within the limit of the convergence tolerances with respect to τ_{SCNC}, presumably as a result of a rather flat potential energy surface and bias from the initial coordinates. Convergence was achieved more rapidly as pressure was increased and volume reduced, restricting the range of energetically favourable conformations. Despite the conformational degeneracy at lower pressures, there were still clear pressure-dependent trends in the torsion angles, so fits to these were performed across the pressure series and the resulting fits were used as restraints on the powder data refinements—i.e. restraining the torsion angles to the values fitted against the data. Torsion angle plots, and the corresponding fits are available in the ESI†.

4.2 Molecular flexibility and motion in the crystal

The intramolecular flexibility shown by ROY is demonstrated clearly by the effect of pressure. However, this gives a time-average picture where the only indication of deviation from the average is reflected by the size of the atomic ADPs. To get more insight into the dynamics of the molecule in the crystal, we can make use of the information present in our multi-temperature single-crystal neutron diffraction data. A normal coordinate analysis—using the method described in ref. 29—can help in recognising the dominant low-energy normal modes affecting the magnitude of the ADPs, i.e. those responsible for the molecular deformations. In addition, this method isolates the contributions to the ADPs that arise from high-frequency optical modes, in the form of an additive tensor that can be refined for each atomic species.

The starting point of the normal coordinate analysis is to determine the deviation from rigidity of the molecule by fitting a rigid-body description of the ADPs via a least-squares minimisation. The model of motion consists of the six 'external' lattice vibrations—the three translations and three librations of the Schomaker and Trueblood TLS description,[47]—but using only a set of six frequencies, and the corresponding six eigenvectors, to describe all the ADPs at all measured temperatures. The point symmetry of the ROY molecule is C_1 and therefore libration and translation eigenvector components are allowed to mix.*

This model resulted in translational and librational frequencies with the expected range of values: around 30 cm^{-1} for translations, 63(3) cm^{-1} for libration about x L_x, and 42(1) cm^{-1} for a combination of libration about z and translation along x (L_z, T_x), contributing 78% and 22%, respectively. A final agree-

* In the Schomaker and Trueblood description, this means that the screw tensor is non-zero. In the normal coordinate analysis used here, the description of a motion composed of more than one normal mode is obtained by the refinement of one frequency (i.e. eigenvalue) and its corresponding multi-component eigenvector.

ment factor of 17%, and an undetermined frequency for L_y, attested that more flexibility had to be included in the model. The model of motion was therefore modified in such a way that additional eigenvector components which accounted for rotation about τ_{SCNC} and a simultaneous in-phase, out-of-plane displacement of the NH and NO_2 groups, were allowed to refine. The fit improved to an agreement of 11% and the previously-undetermined L_y frequency could be refined to 123(35) cm^{-1} with eigenvector components indicating a strong coupling of L_y (51%) with τ_{SCNC} (44%), making this torsion the most significant low-energy deformation contributing to the ADPs.

4.3 Effect of pressure and temperature on lattice energies

The lattice energies of seven of the eight ROY polymorphs have been evaluated previously using CE-B3LYP calculations and also the PIXEL method, using electron density calculated at the MP2/6-31G(d,p) level.[48,49] Although each study differed slightly in assigning relative polymorph stabilities, they agree that the Y form is the most stable and that the overall lattice energy difference between the most and least stable (ORP or ON) polymorphs is *ca.* 13 $kJmol^{-1}$, although some of the energy differences between intermediate-stability forms are less than 1 $kJmol^{-1}$. This is consistent with the experimental evidence that there is near-degeneracy in polymorph energies at ambient conditions. We have now performed PIXEL calculations to explore the effect of non-ambient pressures and temperatures on the intermolecular forces and lattice energies in the OP form, motivated by the fact that non-ambient conditions frequently drive phase transitions in other organic materials by altering the hierarchy of polymorph stabilities. Furthermore, as structural models are available from the earlier high-pressure study of the thermodynamically-favoured Y form,[13] we have analysed these with PIXEL also, and are able to contrast its pressure-induced behaviour with that of the OP-form.

Between 293 and 40 K, the total calculated lattice energy changes very little, decreasing progressively from −134.9 to −146.1 $kJmol^{-1}$, respectively, thus becoming more stable as temperature is reduced. As the PIXEL approach cannot process partial occupancies, for all temperatures where more than one methyl orientation was identified, energies were calculated using fully-ordered crystal structures in each orientation. The resulting energies were then scaled according to the refined occupancies, obtaining a weighted average energy for each temperature. The impact of methyl reorientation was, however, rather limited, where the greatest difference it made on total lattice energy was 0.9 $kJmol^{-1}$ at 293 K and 60 K, 0.5 $kJmol^{-1}$ at 100 K, and 0.3 $kJmol^{-1}$ at 150 K. Owing to the relatively subtle influence of temperature on the crystal structure, we will now focus on the more pronounced pressure-driven changes.

In our earlier study of the Y form of ROY, we found that the crystal did not undergo any structural transitions.[13] Instead it became a compressed form of the ambient phase and steadily changed colour due to increased ring conjugation as the nitrophenyl and thiophenecarbonitrile groups tended towards coplanarity. The same structural behaviour has been observed for the OP phase in this study—indeed the compression characteristics are extremely similar as the OP and Y forms possess comparable bulk moduli: 4.3(3)/6.0(7) GPa, respectively; and first derivatives: 15.3(9)/11.1(12). Although the unit cell volumes of each phase are reduced by similar amounts, the Y-form remains the more efficiently packed; using the relevant equation of state for each phase, at 5.1 GPa, the OP cell volume is 931.8 $Å^3$, and in Y, it is 916.8 $Å^3$. This 15 $Å^3$ difference, while small, is significant—energetically, this corresponds to a pressure×volume reward of 11.5 $kJmol^{-1}$ per molecule, towards Gibbs free energy.

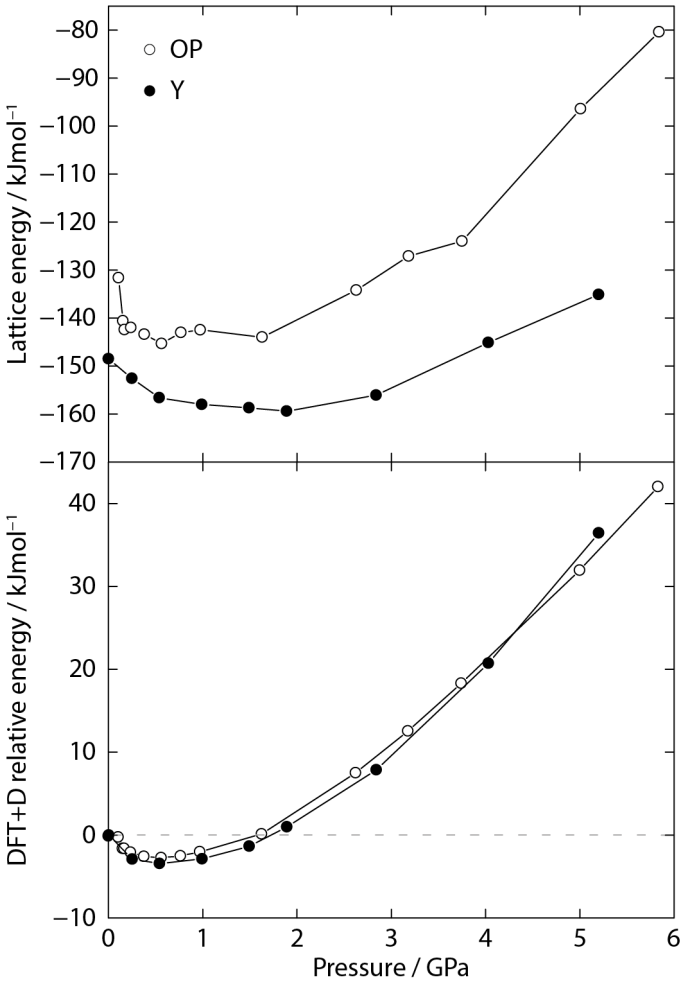

Fig. 5 Top: Total lattice energies, per molecular unit, calculated using PIXEL for the OP and Y phases of ROY, as a function of pressure. Bottom: Change in dispersion-corrected DFT energy, relative to ambient pressure, for fixed-cell geometry optimisations of both phases. Energies shown are per molecule. The OP ambient pressure point was calculated using the coordinates and unit cell dimensions of CSD structure QAXMEH03 as a starting point.

Figure 5 shows calculated lattice energies per molecular unit as a function of pressure, for both forms, and Figure 6 shows the most influential molecule–molecule dimer energies (within a cluster radius of 20 Å, over which the calculation is performed) as a function of centroid–centroid distance. Lattice energies are given in Table 2. The first point to note is that the PIXEL lattice energies show that Y remains the more stable, and is increasingly so

Table 2 PIXEL lattice energies for OP- and Y-ROY. All energies are given in kJmol^{-1}

Phase	P / GPa	E_{Coul}	E_{pol}	E_{disp}	E_{rep}	E_{tot}
OP	0.11	−51.6	−22.8	−158.6	+101.3	−131.6
OP	0.15	−46.9	−18.1	−158.3	+82.7	−140.6
OP	0.17	−46.1	−17.3	−157.2	+78.1	−142.4
OP	0.24	−50.0	−20.4	−164.8	+93.1	−142.0
OP	0.38	−53.9	−21.8	−172.2	+104.6	−143.4
OP	0.56	−60.7	−25.8	−183.3	+124.6	−145.3
OP	0.77	−68.3	−30.0	−195.2	+150.5	−143.0
OP	0.97	−75.5	−33.7	−203.4	+170.2	−142.5
OP	1.63	−89.0	−40.1	−227.2	+212.2	−144.0
OP	2.63	−108.0	−53.1	−259.2	+286.1	−134.2
OP	3.19	−124.5	−62.3	−275.1	+334.8	−127.1
OP	3.75	−131.4	−64.9	−287.8	+360.1	−124.0
OP	5.01	−168.1	−86.6	−317.2	+475.5	−96.4
OP	5.84	−190.4	−98.9	−334.5	+543.4	−80.4
Y	0.0	−43.7	−18.9	−154.9	+69.0	−148.5
Y	0.25	−61.1	−29.3	−182.0	+119.8	−152.6
Y	0.54	−67.8	−33.1	−193.2	+137.5	−156.6
Y	0.99	−81.1	−40.4	−215.4	+178.9	−158.0
Y	1.49	−92.7	−47.7	−235.3	+217.0	−158.7
Y	1.89	−98.8	−52.2	−249.0	+240.6	−159.4
Y	2.84	−119.4	−65.2	−276.4	+304.8	−156.1
Y	4.03	−147.3	−83.4	−309.9	+395.5	−145.1
Y	5.20	−173.4	−101.0	−337.1	+476.3	−135.1

at higher pressures while OP becomes rapidly less stable. In fact, over the course of compression, the lattice energy for Y changes relatively little, increasing from −148.5 to −135.1 kJmol^{-1} between ambient pressure and 5.2 GPa, whereas the OP lattice energy increases by *ca.* 50 kJmol^{-1} going from −131.6 kJmol^{-1} at 0.1 GPa to −80.4 kJmol^{-1} by 5.8 GPa. The OP lattice energy appears to undergo a rapid initial decrease above 0.1 GPa, as pressure is increased—this may simply be due to C-H distances being fixed to 1.1 Å for this single dataset, owing to unstable refinement; small modifications to atomic positions can lead to changes of several kJmol^{-1} in PIXEL energies. However, the general pressure dependence of both OP and Y-form lattice energies is clear—an overall increase in energy, preceded by an apparent stabilisation (relative to the ambient pressure form), when modest pressure is applied.

The initial stabilisation with pressure is counter-intuitive, but is independently confirmed by the internal energies predicted by the DFT optimisations, which show the same trend as PIXEL—see Figure 5, lower panel (although at ambient pressure, the calculations find the OP form to be ca. 3.2 kJmol^{-1} more stable than Y). This behaviour is not without precedent—other studies have made similar observations.[50] The authors of ref. 50 showed that this could be compensated for by changes in intramolecular conformation and pressure×volume contributions to Gibbs free energy. In our case, gas phase, single-point energy calculations of ROY relative to ambient pressure (effectively identifying energy change due to conformation), proved inconclusive—likely due to refined bond lengths and angles fluctuating within experimental error between pressure points. However, the same approach using DFT-optimised structures, resulted in small increases to the DFT internal energy over the 'stabilised' low-pressure region; up to 2.7 and 3.2 kJmol^{-1} in OP and Y-ROY, respectively (see ESI†for details). After correction, negative relative energies, above room pressure, are reduced to ca. 2 kJmol^{-1}, which we suggest are the result of thermally-influenced energy terms that are unaccounted for by the calculations here. Further correction—to include the work performed by pressure on the cell volume—shows that enthalpy increases almost linearly as a function of pressure (see ESI†). So, in summary, although lattice energy decreases initially with pressure, this is partially counteracted by unfavourable changes in molecular conformation, which are stabilised by the need to minimise volume, and this leads ultimately to a continuous increase in Gibbs free energy.

Table 3 PIXEL dimer symmetry relationships to a reference molecule at x,y,z in OP and Y-phase ROY, for interactions ≥ 15 kJmol^{-1}. Note there is no relation between dimers with the same code in different polymorphs.

Dimer code	Sym. operation OP	Sym. operation Y
a	$x-\frac{1}{2},\bar{y}+\frac{3}{2},z-\frac{1}{2}$	$\bar{x}+1,\bar{y}+1,\bar{z}+1$
b	$\bar{x},\bar{y}+1,\bar{z}+1$	$\bar{x}+2,\bar{y}+1,\bar{z}+1$
c	$x-\frac{1}{2},\bar{y}+\frac{3}{2},z+\frac{1}{2}$	$x-\frac{1}{2},\bar{y}+\frac{1}{2},z+\frac{1}{2}$
d	$\bar{x}-\frac{1}{2},y-\frac{1}{2},\bar{z}+\frac{3}{2}$	$x,y,z-1$
e	$\bar{x},\bar{y}+1,\bar{z}+2$	$x-\frac{1}{2},\bar{y}+\frac{1}{2},\bar{z}-\frac{1}{2}$
f	$\bar{x},\bar{y}+2,\bar{z}+1$	$\bar{x}+1,\bar{y}+1,\bar{z}+2$
g	$\bar{x}+\frac{1}{2},y-\frac{1}{2},\bar{z}+\frac{3}{2}$	$x-1,y,z$
h	$\bar{x}-\frac{1}{2},y-\frac{1}{2},\bar{z}+\frac{1}{2}$	n/a

4.4 Intermolecular energies

Select intermolecular energies between pairs of molecules, as a function of molecule–molecule centroid distance, are shown in the upper panels of Figure 6. Each interaction is labelled alphabetically, and the symmetry relationship for each interaction (from a molecule at x,y,z) is given in Table 3. In the Y form, the most stabilising interaction (which we denote $\mathrm{Y_A}$) is that between the $\pi\cdots\pi$ stacked dimers, related by the inversion operator at the cell body centre, however, this changes very little over the course of compression. This largely dispersive interaction dominates over all others, as represented pictorially in the lower panels of Figure 6. Here, we represent the interactions graphically using 'hedgehog'-vectors developed by Shishkin et al, and implemented in processPIXEL—vector lengths represent interaction strength and are scaled relative to the largest energy, thus the most stabilising interaction is an unbroken line between two molecules.[28,51] There are only two other interactions of note—$\mathrm{Y_B}$ which generally becomes more stabilising, until the very highest pressure of 5.2 GPa, and $\mathrm{Y_C}$ which shows the inverse behaviour, becoming less stabilising by approximately the same magnitude.

The situation is rather different in OP where there is no single stabilising intermolecular interaction comparable to that of $\mathrm{Y_A}$. Furthermore, the two most stabilising interaction energies $\mathrm{OP_A}$ and $\mathrm{OP_B}$, which lie between the closest pairs of neighbouring molecules, become rapidly less stabilising as pressure is increased, increasing by +14.8 and +20.5 kJmol^{-1}, respectively. The same is true to a lesser extent of $\mathrm{OP_C}$. Like most interactions in the ROY polymorphs reported by Dunitz and Gavezzotti,[49] $\mathrm{OP_A}$ and $\mathrm{OP_C}$ are mostly comprised of dispersive contributions, however, the balance of forces in $\mathrm{OP_B}$ changes over the pressure series—initially a small majority is attributable to dispersion, however by 5.8 GPa, there is a fairly even contribution

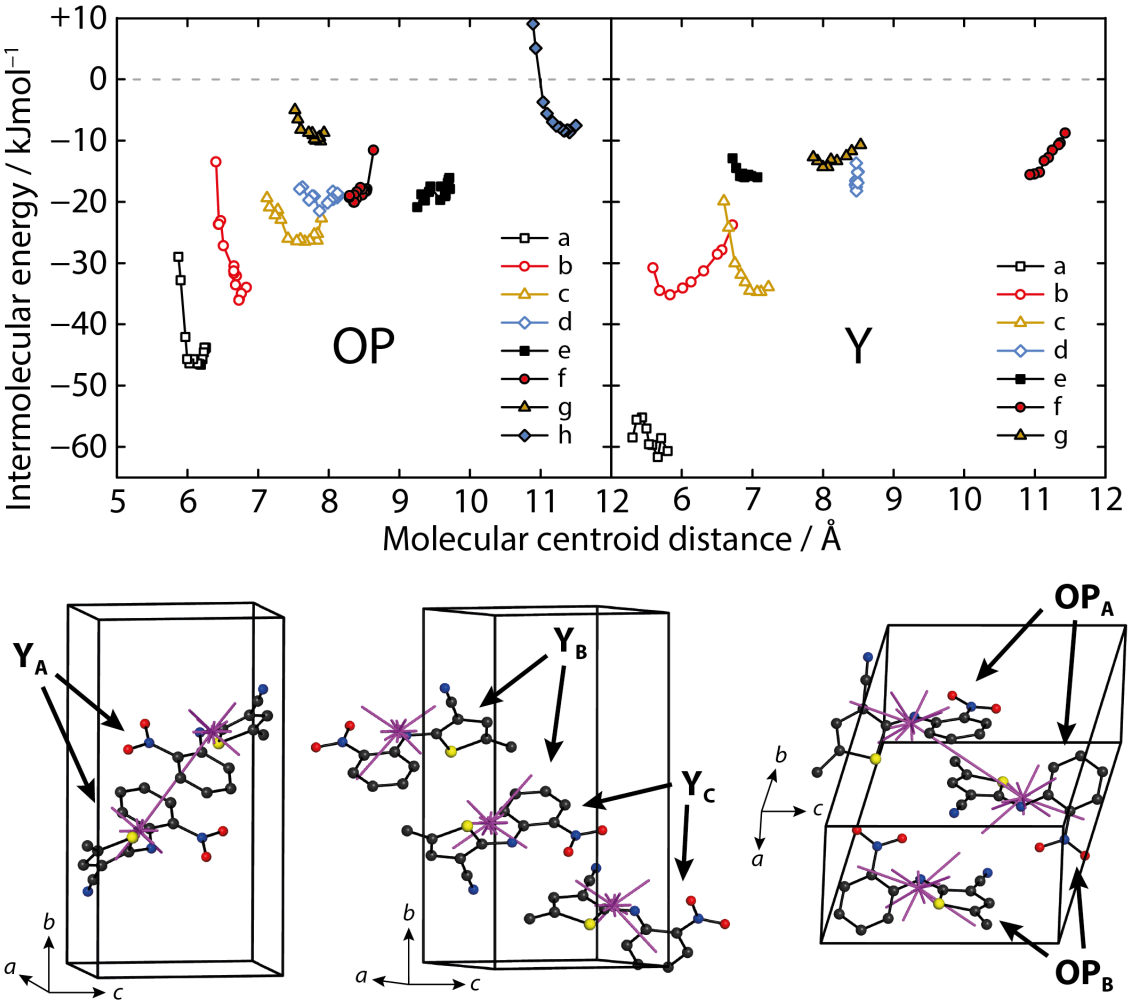

Fig. 6 Top: Specific molecule–molecule dimer total energies, calculated using PIXEL. Energies are shown as a function of distance between molecule–molecule centres of mass (calculated omitting hydrogen atoms). The dotted line indicates the point above which interactions become destabilising. Symmetry operations for each specific dimer are given in Table 3. Bottom, from left to right: specific molecule–molecule contacts Y_A, Y_B, Y_C, OP_A, and OP_B with 'hedgehog' vector diagrams shown in purple, originating from molecular centres of mass. H atoms are omitted for clarity.

from both Coulombic and dispersive forces. There is an additional interaction (denoted 'h' in the top plot) that appears to become a slightly destabilising force (i.e. positive energy) at higher pressures that originates between two molecules where a nitrile group is in close proximity to a neighbouring methyl group. We are, however, tentative in interpreting this as a repulsive force, rather than weakly-attractive, due to the afore-mentioned issues with the influence of hydrogen positions on the calculation and knowing absolute energies.

Rapid increases in molecular dimer energies have explained pressure-driven transitions in other organic systems, for example salicylaldoxime and hydroquinone–methanol/acetonitrile clathrates,[52,53] where the interactions become sufficiently destabilising (or less stabilising) to drive transformation to another crystalline form. As no phase transition was observed up to 5.8 GPa despite a sharp increase in dimer energies, we explored the effect of pressure up to 9.3 GPa. Although the data quality was not sufficient for Rietveld refinement, and therefore nor PIXEL analysis, the pattern was determined unambiguously to contain only OP ROY—its intermolecular interactions are still sufficiently stabilising. Should barriers to transformation prove insurmountable by hydrostatic compression, the OP phase may simply become amorphous at higher pressures still, as seen in some other organics and framework materials.[54–56]

4.5 Compression mechanism

The OP molecular conformation is closer to planarity at ambient conditions than that of the Y form, and evidently its key torsion angle is less amenable to pressure-induced change (OP $\Delta\tau = 17.9°$ *c.f.* 28.2° in Y), however, its overall crystal structure is more compressible. Flexibility through molecular conformation was identified as a key aspect in the compression of the Y-form, in combination with a wine-rack-style lattice deformation.[13] The latter of these is still a contributing factor in OP ROY, and flattening of the molecule (see Figure 4, right-hand panels) is most likely to affect packing along the $\mathbf{X}_1$ direction—the most compressible principal axis. We also note that the less compressible $\mathbf{X}_2$ axis is aligned with the strongest intermolecular interaction, OP_A, and that the

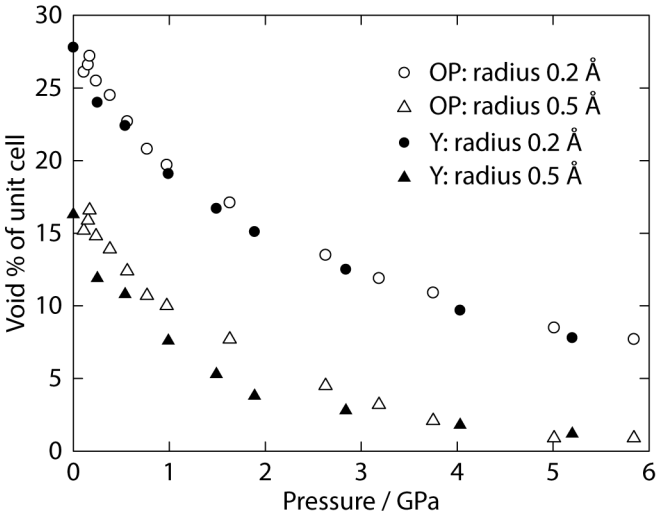

Fig. 7 Percentage of unoccupied unit cell volume as a function of pressure. Open symbols correspond to the OP phase, filled symbols to Y. Circles indicate a probe radius of 0.2 Å, triangles indicate 0.5 Å

behaviour of $\mathbf{X}_3$ is not clearly related to any single molecule–molecule feature. In the absence of any other intramolecular distortions, the voids between molecules must simply be contracting in order to reduce volume. Although, ultimately, compression of the Y form also proceeds via void reduction, as is typical of most organic crystals, it is the distribution of voids that differs significantly between the two forms, promoting differences in conformational behaviour.

Available void space as a function of pressure was calculated using Mercury CSD 3.9 using different-sized probe radii (of spheres that can be located in the structure, without occupying the same space as any atom) and is plotted in Figure 7. The smallest available probe radius, 0.2 Å, provides the closest estimate of total available void space, as a percentage of unit cell volume, and shows that there is very little difference between the two forms. However, increasing the size of the probe radius to 0.5 Å shows that between *ca.* 1 and 3 GPa there are larger, and therefore more concentrated, voids in the OP form—this is shown visually in the ESI†. Over this pressure range, in order to best access their relative void volumes, the molecules move closer together and rotate to differing extents in OP and Y.

5 Conclusions

We find that the molecular packing of OP ROY is very compressible, having a small bulk modulus of 4.3(3) GPa, yet remains kinetically trapped as no transition is observed up to 9.3 GPa, retaining the same $P2_1/n$ symmetry seen at ambient conditions. Furthermore, it persists to temperatures of 40 K. It is remarkable that a material which shows such polymorphic behaviour under ambient conditions has not yet yielded new, or transitions to currently known, phases with pressure or temperature stimuli. This is not a trait that is necessarily typical of concomitant polymorphs; the α, β, and γ forms of glycine can all be obtained at ambient pressure and temperature but their behaviour under pressure differs enormously—β and γ-glycine transform at pressures below 4 GPa, whereas α-glycine persists to at least 23 GPa.[57–60] Indeed in the ROY system itself, there are clear differences between stabilities of the various forms—some of the metastable polymorphs survive weeks to months, and others hours to days.[10] This also suggests that the behaviour of the OP and Y forms is not necessarily indicative of how the remaining ROY phases will respond, which have very different structures and thus different energy barriers to conversion. This, coupled with the ability to pressurise the crystal structures such that their lattice energies become very different, as shown by our PIXEL calculations, means it would be very interesting to observe the influence of pressure on some the less stable forms.

6 Conflicts of interest

There are no conflicts to declare.

7 Acknowledgements

We thank Dr Dominic Fortes for assistance with the DFT calculations, Dr Andrew Bond for guidance with processPIXEL, and ISIS and STFC for providing access to the PEARL and SXD instruments. Computing resources were provided by the STFC Scientific Computing Department's SCARF cluster.

References

1 S. L. Price, *Chem.Soc. Rev.*, 2014, **43**, 2098–2111.
2 J. Bernstein, *Polymorphism in Molecular Crystals*, Oxford University Press, Oxford, UK, 2002.
3 J. A. Foster, K. K. Damodaran, A. Maurin, G. M. Day, H. P. G. Thompson, G. J. Cameron, J. Cuesta Bernal and J. W. Steed, *Chem. Sci.*, 2017, **8**, 78–84.
4 A. J. Cruz-Cabeza and J. Bernstein, *Chem. Rev.*, 2014, **114**, 2170–2191.
5 Y. Diao, K. E. Whaley, M. E. Helgeson, M. A. Woldeyes, P. S. Doyle, A. S. Myerson, T. A. Hatton and B. L. Trout, *J. Am. Chem. Soc.*, 2012, **134**, 673–684.
6 D. S. Coombes, C. R. A. Catlow and B. Slater, *Mol. Simul.*, 2008, **34**, 873–877.
7 J. J. McKinnon, F. P. A. Fabbiani and M. A. Spackman, *Cryst. Growth Des.*, 2007, **7**, 755–769.
8 M. Vasileiadis, A. V. Kazantsev, P. G. Karamertzanis, C. S. Adjiman and C. C. Pantelides, *Acta Crystallogr.*, 2012, **B68**, 677–685.
9 J. L. Hilden, C. E. Reyes, M. J. Kelm, J. S. Tan, J. G. Stowell and K. R. Morris, *Cryst. Growth Des.*, 2003, **83**, 921–926.
10 L. Yu, *Acc. Chem. Res.*, 2010, **43**, 1257–1266.
11 M. Tan, A. Shtukenberg, S. Zhu, W. Xu, E. Dooryhee, S. M. Nichols, M. D. Ward, B. Kahr and Q. Zhu, *Faraday Discuss.*, 2018.
12 S. Chen, H. Xi and L. Yu, *J. Am. Chem. Soc.*, 2005, **127**, 17439–17444.
13 E. L. Harty, A. R. Ha, M. R. Warren, A. L. Thompson, D. R. Allan, A. L. Goodwin and N. P. Funnell, *Chem. Commun.*, 2015, **51**, 10608–10611.

14 C. L. Bull, N. P. Funnell, M. G. Tucker, S. Hull, D. J. Francis and W. G. Marshall, *High Pressure Res.*, 2016, **36**, 493–511.

15 W. G. Marshall and D. J. Francis, *J. Appl. Crystallogr.*, 2002, **35**, 122–125.

16 J. M. Besson, R. J. Nelmes, G. Hamel, J. S. Loveday, G. Weill and S. Hull, *Phys. B*, 1992, **180**, 907–910.

17 O. Arnold, J. C. Bilheux, J. M. Borreguero, A. Buts, S. I. Campbell, L. Chapon, M. Doucet, N. Draper, R. Ferraz Leal, M. A. Gigg, V. E. Lynch, A. Markvardsen, D. J. Mikkelson, R. L. Mikkelson, R. Miller, K. Palmen, P. Parker, G. Passos, T. G. Perring, P. F. Peterson, S. Ren, M. A. Reuter, A. T. Savici, J. W. Taylor, R. J. Taylor, R. Tolchenov, W. Zhou and J. Zikovsky, *Nucl. Instrum. Meth. A*, 2014, **764**, 156–166.

18 D. A. Keen, M. J. Gutmann and C. C. Wilson, *J. Appl. Crystallogr.*, 2006, **39**, 714–722.

19 M. J. Gutmann, *Nucl. Instrum. Meth. A*, 2017, **848**, 170–173.

20 M. J. Gutmann, *SXD2001*, 2005.

21 S. J. Clark, M. D. Segall, C. J. Pickard, P. J. Hasnip, M. J. Probert, K. Refson and M. C. Payne, *Z. Krist.*, 2005, **220**, 567–570.

22 J. P. Perdew, K. Burke and E. M, *Phys. Rev. Lett.*, 1996, **77**, 3865–3868.

23 S. Grimme, *J. Comput. Chem.*, 2006, **27**, 1787–1799.

24 D. Vanderbilt, *Phys. Rev. B*, 1990, **41**, 7892–7895.

25 M. J. Frisch, G. W. Trucks, H. B. Schlegel, G. E. Scuseria, M. A. Robb, J. R. Cheeseman, G. Scalmani, V. Barone, B. Mennucci, G. A. Petersson, H. Nakatsuji, M. Caricato, X. Li, P. Hratchian, A. F. Izmaylov, J. Bloino, G. Zheng, J. L. Sonnenberg, M. Hada, M. Ehara, K. Toyota, R. Fukuda, J. Hasegawa, M. Ishida, T. Nakajima, Y. Honda, O. Kitao, H. Nakai, T. Vreven, J. A. Montgomery Jr., J. E. Peralta, F. Ogliaro, M. Bearpark, J. J. Heyd, E. Brothers, K. N. Kudin, V. N. Staroverov, T. Keith, R. Kobayashi, J. Normand, K. Raghavachari, A. Rendell, J. C. Burant, S. S. Iyengar, J. Tomasi, M. Cossi, N. Rega, J. M. Millam, M. Klene, J. E. Knox, J. B. Cross, V. Bakken, C. Adamo, J. Jaramillo, R. Gomperts, R. E. Stratmann, O. Yazyev, A. J. Austin, R. Cammi, C. Pomelli, J. W. Ochterski, M. R. L, M. K, V. G. Zakrzewski, G. A. Voth, P. Salvador, J. J. Dannenberg, S. Dapprich, A. D. Daniels, O. Farkas, J. B. Foresman, J. V. Ortiz, J. Cioslowski and D. J. Fox, *Gaussian09, Revision D01*, 2013.

26 A. Gavezzotti, *J. Phys. Chem.*, 2003, **B107**, 2344–2353.

27 A. Gavezzotti, *Mol. Phys.*, 2008, **106**, 1473–1485.

28 A. D. Bond, *J. Appl. Cryst.*, 2014, **47**, 1777–1780.

29 Bürgi, H B and Capelli, S C, *Acta Crystallogr.*, 2000, **A56**, 403–412.

30 Bürgi, H B and Förtsch, M and Capelli, S and Hauser, J, *NKA: Program for normal coordinate analysis from anisotropic displacement parameters at multiple temperatures, v. 5.1.17*, 2004.

31 A. Coelho, *Topas V5.0*, 2014.

32 C. R. Groom, I. J. Bruno, M. P. Lightfoot and S. C. Ward, *Acta Crystallogr.*, 2016, **B72**, 171–179.

33 G. M. Sheldrick, *Acta Crystallogr.*, 2015, **C71**, 3–8.

34 M. T. Weller, P. F. Henry, V. P. Ting and C. C. Wilson, *Chem. Commun.*, 2009, **7345**, 2973.

35 I. Majerz, Z. Malarski and T. Lis, *J. Mol. Struct.*, 1990, **240**, 47–58.

36 J. Zhou, Y.-S. Kye and G. S. Harbison, *J. Chem. Am. Soc.*, 2004, **126**, 8392–8393.

37 S. Crawford, M. T. Kirchner, D. Bläser, R. Boese, W. I. F. David, A. Dawson, A. Gehrke, R. M. Ibberson, W. G. Marshall, S. Parsons and O. Yamamuro, *Angew. Chem. Int. Ed.*, 2009, **48**, 755–757.

38 C. Shi, X. Zhang, C.-H. Yu, Y.-F. Yao and W. Zhang, *Nat. Commun.*, 2018, **9**, 481.

39 J. Falk, D. Hofmann and K. Merz, *IUCrJ*, 2018, **5**, in press.

40 P. F. Henry, M. T. Weller and C. C. Wilson, *J. Appl. Crystallogr.*, 2009, **42**, 1176–1188.

41 C. C. Wilson, P. F. Henry, M. Schmidtmann, V. P. Ting, E. Williams and M. T. Weller, *Crystallogr. Rev.*, 2014, **20**, 162–206.

42 I. B. Hutchison, C. L. Bull, W. G. Marshall, S. Parsons, A. J. Urquhart and I. D. H. Oswald, *Acta Crystallogr.*, 2017, **B73**, 1151–1157.

43 F. Birch, *Phys. Rev.*, 1947, **71**, 809–824.

44 M. J. Cliffe and A. L. Goodwin, *J. Appl. Crystallogr.*, 2012, **45**, 1321–1329.

45 N. P. Funnell, A. Dawson, D. Francis, A. R. Lennie, W. G. Marshall, S. A. Moggach, J. E. Warren and S. Parsons, *CrystEngComm*, 2010, **12**, 2573–2583.

46 J. Binns, M. R. Healy, S. Parsons and C. A. Morrison, *Acta Crystallogr.*, 2014, **B70**, 259–267.

47 V. Schomaker and K. N. Trueblood, *Acta Crystallogr.*, 1968, **B24**, 63–76.

48 S. P. Thomas and M. A. Spackman, *Aust. J. Chem.*, 2018, **71**, 279–284.

49 J. D. Dunitz and A. Gavezzotti, *Cryst. Growth Des.*, 2005, **5**, 2180–2189.

50 P. A. Wood, D. A. Haynes, A. R. Lennie, W. D. S. Motherwell, S. Parsons, E. Pidcock and J. E. Warren, *Cryst. Growth. Des.*, 2008, **8**, 549–558.

51 O. V. Shishkin, V. V. Dyakonenko and A. V. Maleev, *CrystEngComm*, 2012, **14**, 1795–1804.

52 P. A. Wood, R. S. Forgan, D. Henderson, S. Parsons, E. Pidcock, P. A. Tasker and J. E. Warren, *Acta Crystallogr.*, 2006, **B62**, 1099–1111.

53 E. Eikeland, M. K. Thomsen, J. Overgaard, M. A. Spackman and B. B. Iversen, *Cryst. Growth. Des.*, 2017, **17**, 3834–3846.

54 N. P. Funnell, W. G. Marshall and S. Parsons, *CrystEngComm*, 2011, **13**, 5841–5848.

55 T. Okumura, M. Ishida, K. Takayama and M. Otsuka, *J. Pharm. Sci.*, 2006, **95**, 689–700.

56 T. D. Bennett, P. Simonic, S. A. Moggach, F. Gozzo, P. Macchi, D. A. Keen, J.-C. Tan and A. K. Cheetham, *Chem. Commun.*, 2011, **47**, 7893–7985.

57 C. Murli, S. M. Sharma, S. Karmakar and S. K. Sikka, *Phys. B: Cond. Matter*, 2003, **339**, 23–30.

58 S. V. Goryainov, E. N. Kolesnik and E. V. Boldyreva, *Phys. B: Cond. Matter*, 2005, **357**, 340–347.
59 E. V. Boldyreva, S. N. Ivashevskaya, H. Sowa, H. Ahsbahs and H.-P. Weber, *Z. Kristallogr*, 2005, **220**, 50–57.
60 S. A. Moggach, S. Parsons and P. A. Wood, *Crystallogr. Rev.*, 2008, **14**, 143–184.